Nuclear Materials and Energy 47 (2026) 102116

Contents lists available at ScienceDirect

Nuclear Materials and Energy

journal homepage: www.elsevier.com/locate/nme

Liquid Sn compatibility of HiPIMS W-based multilayers: Influence of coating architecture and substrate finish☆

D. Vavassori [a,1,*], L. Bana [a,1], M. Bugatti [a,b,1], F. Zarotti [b], N. Lecis [c], M. Iafrati [b], M. Passoni [a,d], L. Ferrante [b], D. Dellasega [a,d,*]

[a] Politecnico di Milano, Department of Energy, via R. Lambruschini 8, Milano, Italy
[b] Department of Fusion and Technology for Nuclear Safety and Security, ENEA, Via E. Fermi 45, Frascati, Italy
[c] Politecnico di Milano, Department of Mechanical Engineering, Via Privata G. La Masa 1, 20156 Milano, Italy
[d] Istituto per la Scienza e Tecnologia dei Plasmi (ISTP) - CNR, via R. Cozzi 53, Milano, Italy

ABSTRACT

The use of liquid tin divertors in future nuclear fusion devices requires effective solutions to mitigate corrosion of structural materials. In this work, tungsten-based coatings deposited by High Power Impulse Magnetron Sputtering (HiPIMS) were investigated as protective barriers for CuCrZr alloys used in fusion heat sink components. The study aimed to identify the key material and engineering parameters governing coating performance under liquid tin exposure. Multilayer coatings with different compositions (tungsten–aluminium, tungsten–nitrogen and tungsten–chromium–titanium), architectures and morphologies were tested using static liquid tin corrosion experiments at 400 °C. Coating adhesion was evaluated prior to corrosion, while morphological and microstructural analyses were performed before and after exposure. Concerning tungsten-aluminium coatings, additional tests at 500 °C assessed the influence of coating thickness and substrate roughness. All tungsten-based coatings exhibited excellent chemical compatibility with liquid tin, with degradation primarily driven by mechanical and morphological factors. Coatings containing amorphous mixed layers showed superior corrosion resistance, attributed to the absence of grain boundaries and improved mechanical compliance. Multilayer architectures further enhanced robustness, while fully crystalline layers were more susceptible to brittle failure. Coating thickness and substrate surface finish were identified as critical parameters for reliable protection. The presented results are valuable to design protective coatings for liquid tin divertor applications and to support the transition toward reactor-relevant fusion components.

Introduction

The use of liquid metals in the nuclear power sector has been explored since its early development [1,2]. Liquid metals have attracted interest due to their unique physical properties, which offer potential advantages for nuclear applications. While liquid metals have been extensively investigated in fission systems, their role in fusion devices is still at an early stage [3]. Specifically, they are considered promising for the development of novel first-wall and plasma-facing component configurations. Such designs could reduce plasma erosion and enhance tolerance to extreme particle irradiation and heat loads [4,5]. In recent years, these benefits have motivated studies investigating how liquid metals can be practically applied and evaluated from an engineering perspective in future fusion devices, such as the Divertor Tokamak Test facility (DTT) [6–8] and the European DEMOnstration power plant (EU-DEMO) [9–12]. Focusing on the divertor component, ensuring confinement and thermal management of liquid metals within the target region is a fundamental requirement. Among various strategies explored, the Capillary Porous System (CPS), coupled with an underlying heat sink, is currently regarded as the most effective approach for integration in fusion devices, as it allows both liquid metal retention and efficient heat removal [13–15]. With regard to the choice of liquid metal, two main options have been identified: low-Z elements such as lithium (Li), or higher-Z species with low vapour pressure such as tin (Sn). Both have been tested in dedicated experimental devices revealing distinct advantages and limitations [5,11,16–18]. Li offers potential benefits for plasma performance, but presents critical issues, including high fuel retention and oxidation during maintenance periods. In contrast, Sn is attractive due to its low vapour pressure, atmospheric stability and reduced fuel retention. However, as a high-Z element, any penetration into the plasma could result in unwanted radiation losses and cooling.

Additionally, the implementation of a liquid metal divertor requires assessment of other critical aspects, including both physical and

☆ This article is part of a special issue entitled: 'PRD activities' published in Nuclear Materials and Energy.

* Corresponding authors.
E-mail addresses: davide.vavassori@polimi.it (D. Vavassori), david.dellasega@polimi.it (D. Dellasega).

[1] These authors contributed equally to this work as co-first authors.

https://doi.org/10.1016/j.nme.2026.102116
Received 19 December 2025; Received in revised form 27 March 2026; Accepted 1 April 2026
Available online 2 April 2026

engineering constraints. Among these, a major concern common to both liquid Li and Sn is their chemical compatibility with conventional structural materials used in fusion devices (e.g., steels and copper alloys) under the expected operating temperatures [19–26]. In particular, the associated corrosion phenomena represent a serious issue that must be carefully addressed. Focusing on liquid Sn corrosion, previous investigations have highlighted surface coating technology as a viable strategy to mitigate interactions with liquid metals [27–29]. By introducing a properly designed protective coating, the surface properties of structural materials can be tailored without affecting their bulk characteristics. Such an approach proves particularly effective when deposition techniques provide accurate control over key properties including morphology, microstructure and adhesion [30–32]. In this way, coatings can be precisely engineered to improve their stability under the extreme operating regimes characterizing nuclear environments. Nonetheless, several critical aspects related to the use of liquid metals in nuclear fusion applications are still insufficiently explored and require further assessment toward the realization of a valid corrosion barrier. From a fundamental perspective, the interplay between coating chemical composition and its morphology, microstructure or adhesion on protective performances deserves a more detailed and systematic investigation, as demonstrated for liquid metals relevant to fission systems [30,33]. Concurrently, practical and engineering-oriented factors also demand attention. Parameters such as substrate roughness, adhesion at the coating–substrate interface and coating thickness are expected to strongly influence the reliability and operational lifetime of the protective layer in realistic fusion components [29,34]. Specifically, the literature shows that achieving robust adhesion and resistance to tangential stresses on soft and ductile Cu-based substrates requires dedicated strategies, such as interlayers, compositional gradients or multilayer architectures, to compensate for the limited mechanical support of the substrate. This is particularly relevant for refractory metallic or nitride coatings, emphasizing the importance of interfacial engineering for reliable coating performance [35–38].

This work investigates coatings deposited via High Power Impulse Magnetron Sputtering (HiPIMS) [39] as protective barriers for CuCrZr structural alloy employed in the heat sinks of nuclear fusion devices. The study follows a twofold approach, addressing both fundamental materials science aspects and practical engineering considerations. First, building upon knowledge acquired in previous studies [27,40–42], the protective capabilities of multilayered tungsten-based coatings were evaluated through liquid Sn corrosion experiments using a static droplet approach at 400 °C over a duration of 600 min. Specifically, coatings consisting of layers with different compositions (tungsten-aluminium, W-Al; tungsten-nitrogen, W-N; tungsten-chromium-titanium, W-Cr-Ti), as well as coatings with varied multilayer architectures or morphologies, were examined. In alla cases, a proper adhesion strategy was considered to guarantee adequate adhesion to the Cu-based substrate. Second, taking the W-Al system as reference, additional corrosion experiments were conducted at 500 °C for 600 min to further assess the influence of coating thickness and substrate roughness on protective performance. The morphology, microstructure and composition of the coatings were systematically characterized before and after exposure, while adhesion was assessed only prior to corrosion testing. These experiments and analyses provided a more comprehensive understanding of the scientific mechanisms and technological constraints defining the performance requirements of protective coatings. This represents a crucial step toward a transition from proof-of-concept studies to implementation in future liquid metal divertor systems.

Experimental methods

Coatings deposition

For experiments designed to investigate the relationship between composition, morphology and microstructure, different W-based multilayer coatings were deposited using the system described in [43]. Specifically, multilayers containing W-Al, W-N or W-Cr-Ti films were considered. Instead, for experiments focused on coating thickness and substrate roughness, only multilayer W-Al coatings were considered. A representative schematic of the experimental procedure is shown in Fig. 1.

The vacuum chamber was equipped with three confocal cathodes, each loaded with circular elemental sputtering targets (76 mm in diameter, 6 mm in thickness). The targets were ignited using different power supplies and working gases, selected according to the specific coating to be deposited. In all cases, the deposition base pressure was lower than $5{\cdot}10^{-4}$ Pa. The coatings were grown on planar CuCrZr substrates prepared from commercial-grade bulk material, with square or rectangular shapes (10–25 mm in length and width) and thickness fixed to approximately 2 mm. Substrates were ground with SiC papers of different grit sizes and, when required, polished using a 3 μm diamond suspension to achieve final average surface roughness (R_a) levels of approximately 1 μm, 0.5 μm and less than 0.1 μm. Only the finest finish was used in the first set of experiments. Surface oxides and contaminants were removed with metal-cleaning agents, followed by immersion in a solution of anionic and non-ionic surfactants, rinsing with deionized water and final cleaning with isopropanol. For morphology and structure analyses, coatings were also deposited on single-side polished 500 μm thick silicon (100) wafers cleaned with isopropanol. Additional details on the deposition strategies adopted for producing the multielemental coatings are reported in the following paragraphs.

W-Al coatings

Two types of W-Al multilayer coatings were prepared: (i) samples with a single W-Al layer (W-Al#3) and (ii) samples with three W-Al layers (W-Al#7). In both cases, the first step of the process strategy consisted in the deposition of a pure W film (≈80–100 nm in thickness) grown on CuCrZr substrates using a dual-channel SIPP2000 generator (Melec GmbH, Germany) in HiPIMS regime, applying to the substrate 100 μs-long synchronized bias pulses (delay from the main HiPIMS pulse onset $\Delta\tau = 0$ μs, amplitude $U_S = 800$ V). Given the bias amplitude applied, the energetic ion bombardment generated by the highly ionized metallic flux typical of the HiPIMS plasma effectively activates and cleans the substrate surface. Under these conditions, although the bias is relatively high, the deposition rate remains higher than the resputtering rate, enabling the formation of a thin pure W interlayer, which promotes strong interfacial bonding and improved coating adhesion. The same deposition strategy was employed for intermediate and top pure W layers.

For W-Al#3 samples, W and Al cathodes were co-sputtered in HiPIMS mode to form the W-Al layer, followed by a pure W top layer. These coatings were employed in all corrosion experiments. The total thickness was tuned to approximately 1 μm for the first set of tests. Instead, specimens with a W-Al layer thickness of nearly 0.5, 1, 2 and 5 μm were produced to study the influence of coating thickness and substrate roughness on protective performances.

W-Al#7 samples were fabricated only for the first experimental set. Each W-Al layer was of the order of 200 nm in thickness. Between each W-Al layer, a pure W interlayer was deposited and an additional pure W layer was applied on top of the third W-Al layer, resulting in a total of four pure W layers, including the initial bottom layer. The overall thickness resulted of approximately 1 μm. For both pure W and W–Al layers, depositions were carried out in high-purity Ar atmosphere (99.999%), with the working pressure and gas flow rate fixed at 0.5 Pa and 40 sccm, respectively. The full set of deposition parameters is reported in [27]. During W and Al co-deposition, the respective target powers were selected to obtain a nearly equiatomic composition in the resulting mixed layer (≈ 50 at.% W and 50 at.% Al).

W-N coatings

Two types of W–N multilayer coatings were prepared: (i) samples

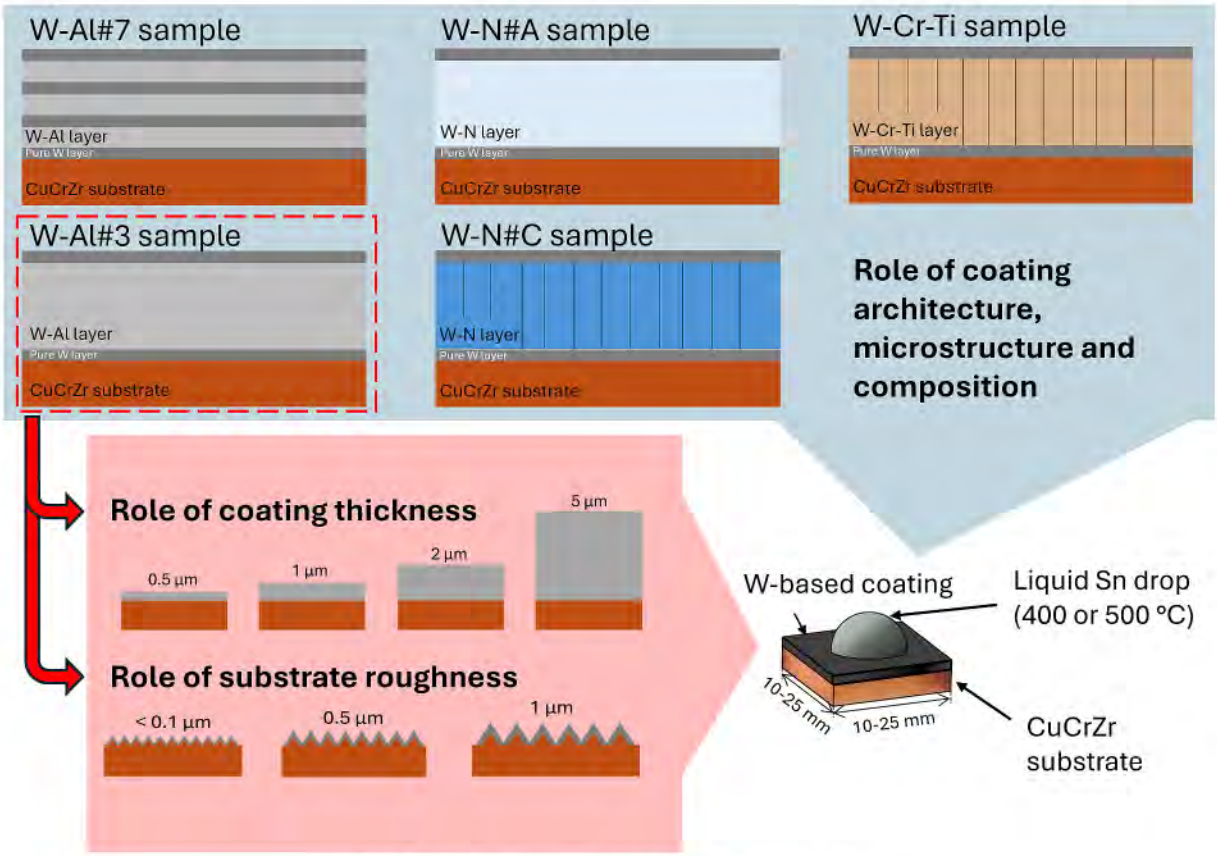

Fig. 1. Summary of the adopted experimental procedure.

consisting of a single crystalline W–N layer (W–N#C) and (ii) samples consisting of a single amorphous W–N layer (W–N#A). In both cases, the W–N layer was sandwiched between two pure W films deposited with the same parameters described in the previous paragraph. The deposition time was adjusted to obtain a total thickness of about 600–700 nm.

For W–N#C samples the vacuum chamber was filled with a mixed N_2 (99.999% purity) and Ar (99.999% purity) atmosphere. The pressure was fixed at 0.5 Pa, while the two inlet gas flows were adjusted to achieve N_2/Ar flow ratio of 25%. The dual-channel SIPP2000 generator supplied a W cathode with 100 µs-long HiPIMS pulses at a duty cycle of 1.75%, maintaining an average power of approximately 230 W.

For W–N#A samples, the mixed N_2-Ar pressure was kept constant at 0.5 Pa, but a N_2/Ar flow ratio equal to 50% was considered. The HiPIMS parameters reported above were adopted to power the W cathode. Additionally, the substrate was biased with delayed and negative 100 µs-long pulses ($\Delta\tau = 60$ µs, $U_S = 400$ V).

More details about W-N layer deposition and characteristics can be found in [41].

W-Cr-Ti coatings

One type of W-Cr-Ti multilayer coating was prepared. The multilayer architecture was designed following the strategy described for W-Al#3 and W-N samples. Thus, the W–Cr-Ti layer was sandwiched between two pure W films deposited with the same parameters described in the paragraph 2.1.1. For the realization of the multi-elemental layer, the deposition chamber was filled with Ar (99.999% purity) up to a working pressure of 0.5 Pa and setting the gas flow to 40 sccm. A Cr, a Ti and a W cathode were co-sputtered. Specifically, the Cr and Ti cathodes were operated in direct current magnetron sputtering (DCMS) mode by one channel of the SIPP2000 power supply and by a single-channel TruPlasma DC 4001 generator (TRUMPF Hüttinger, Germany), respectively. The sputtering power was fixed to 85 W for the Cr cathode and to 250 W for the Ti cathode. The second channel of the SIPP2000 power supply was used to ground the substrate. Instead, a HiPSTER1 power supply (Ionautics AB, Sweden) was used to operate the W cathode in bipolar HiPIMS mode applying 50 µs-long negative voltage pulses at a frequency of 300 Hz (duty cycle of 1.5%). Additionally, 100 µs-long positive pulses with an amplitude of 300 V were applied to the W cathode with minimum delay (1.5 µs) after the negative pulse termination. The average power delivered to the W cathode was approximately 220 W. The deposition time was adjusted to obtain a total thickness of about 600 nm. More details about W-Cr-Ti layer deposition and characteristics can be found in [42].

Corrosion tests

Corrosion tests were carried out in a resistive vacuum oven at ENEA–Centro Ricerche Frascati (Italy). About 1.5 ± 0.1 g of solid Sn (99% purity) was placed on the surface of each sample and confined by an alumina tube (diameter = 10 mm) to fix the interaction area. Sn was then melted in situ during heating in the furnace. For each coated sample, two nominally identical copies were tested in all experiments. The sample configuration described, inserted into an alumina crucible, was heated under vacuum (5×10^{-3} Pa) at 5 °C/min up to 400 or 500 °C and held for 600 min. As demonstrated in our previous work [27], although shorter than the expected divertor component lifetime, this test duration is sufficient to assess the effectiveness of the coating as a diffusion and corrosion barrier during the most critical stages of exposure, given the strong chemical interaction between liquid Sn and Cu. A K-type thermocouple in contact with the sample base monitored the temperature. After exposure, the system was slowly cooled to 50 °C before venting and extracting the samples.

Coatings characterization

The morphological characteristics of the coatings, both before and after corrosion tests, were examined using a LEICA DMI5000 M inverted optical microscope and a Zeiss Supra 40 field emission Scanning Electron Microscope (SEM). Surface morphology and film thickness were studied operating at an accelerating voltage of 5 or 10 kV. For cross-sectional inspection of the interaction region with liquid Sn, samples were embedded in a two-component epoxy resin (Technovit 5017, Kulzer GmbH, Hanau, Germany), sectioned with a silicon carbide rotating blade, polished and cleaned with ethanol.

Elemental composition was investigated via Energy Dispersive X-ray Spectroscopy (EDS) using a Peltier-cooled Silicon Drift Detector (Oxford Instruments), coupled to the previous SEM apparatus, and analyzed with the Aztec software.

Coating/substrate adhesion was evaluated through scratch tests performed using a MCTX S/N 50–0223 (CSM Instruments) equipped with a 200 μm spherical diamond tip Rockwell indenter. During testing, the applied load increased linearly from 0.03 to 30 N at a rate of 10 $N \cdot min^{-1}$ over a scratch length of 3 mm.

Result and discussion

Role of coating architecture, microstructure and composition

Fig. 2 presents the morphological and microstructural characteristics of the as-deposited multilayer coatings. The W-Al#3 coating consists of a featureless and compact central layer sandwiched between two columnar W layers (see Fig. 2(a)). These structures are also observed in the W-Al#7 coating. However, the latter contains a higher number of alternating W and W-Al layers within a comparable total thickness, resulting in a more refined multilayer architecture (see Fig. 2(b)). In both cases, the mixed layers were confirmed to possess an equiatomic composition of W and Al.

For the W-N coatings, a similar configuration is observed, with the mixed W-N layer clearly distinguishable from the two outer W layers. Both the crystalline (W-N#C) and amorphous (W-N#A) coatings show similar central layer morphology. However, in the W-N#C coating a progression from an initially featureless growth to a more ordered structure in the upper region of the layer is observed, consistent with the findings of Bana et al. [41] (see Fig. 2(c)). The composition of the mixed layer resulted approximately 70 at.% W, 25 at.% N and 5 at.% O. In contrast, the W-N#A coating maintains an amorphous-like morphology throughout its thickness, reflecting the deposition conditions optimized to suppress crystallization (i.e., a variation of substrate bias voltage timing). The composition of the mixed layer resulted approximately 65 at.% W, 30 at.% N and 5 at.% O.

The W-Cr-Ti multilayer coating exhibited a columnar and crystalline morphology across all layers (see Fig. 2(d)). According to previous studies [42], the chosen deposition parameters for the multi-metallic layer would have been expected to promote an amorphous film. The fact that columnar growth was instead obtained is likely related to the presence of the underlying columnar W bottom layer. It is reasonable to assume that the crystallographic texture and growth template provided by the initial W layer acted as a seed, promoting oriented growth and thus leading to the observed columnar morphology of the multi-metallic layer. The composition of the mixed layer was found to be approximately equiatomic, with 34 at.% W, 35 at.% Cr and 31 at.% Ti.

All coatings deposited on CuCrZr substrates show good planar uniformity both locally and across larger areas. Even small-scale surface irregularities seem conformally coated, indicating effective step coverage despite the intrinsic roughness of the technical substrates.

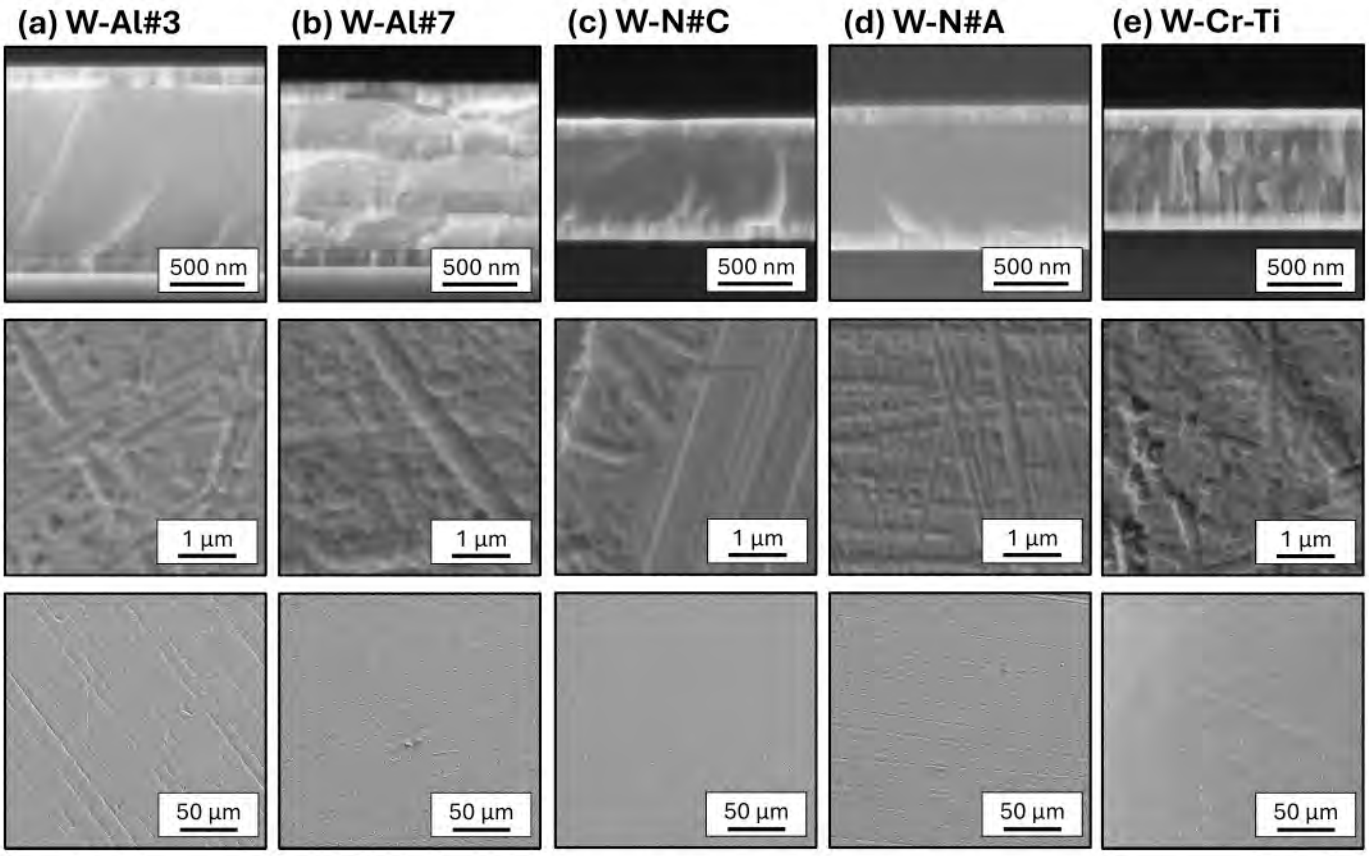

Fig. 2. SEM cross-sectional and planar micrographs of multilayer coatings: **(a)** W-Al#3, **(b)** W-Al#7, **(c)** W-N#C, **(d)** W-N#A and **(e)** W-Cr-Ti. Cross-sectional views correspond to coatings deposited on Si substrates, while planar views (at different magnifications) correspond to coatings deposited on CuCrZr substrates.

The scratch test results are reported in Fig. 3 and the corresponding critical loads are summarized in Table 1. Additional EDS images of the scratch tracks are provided in the Supplementary Material. For all samples, the Cu substrate became visible along at least half of the scratch length, highlighting the significant role of substrate plasticity in transferring stresses to the W-based coatings. Despite this, the influence of coating architecture on adhesion and failure mechanisms can be clearly observed.

The scratch track of a 500 nm-thick pure W coating is shown in Fig. 3 (a) as a reference. This coating, deposited under the same conditions as the bottom/top W layers described in Section 2.1, exhibited predominantly brittle failure, with extensive cracking and spallation along the track. This behaviour indicates that the rigid W coating is unable to accommodate the plastic deformation of the more ductile Cu substrate. Consequently, the measured critical loads for crack initiation (Lc1), coating delamination (Lc2) and full substrate exposure (Lc3) are relatively low.

In contrast, the W-Al#3 coated sample (Fig. 3(b)) displayed improved performance. The amorphous W-Al layer increased the coating effective toughness, dissipating applied stresses and arresting crack propagation. The coating failed in a progressive manner through block-like cracking, without extensive catastrophic spallation, resulting in significantly higher critical loads compared to the pure W coating. A similar behaviour was observed for the W-Al#7 sample (Fig. 3(c)), although slightly lower critical loads were measured. This is likely due to the presence of multiple pure W layers, which increase overall coating stiffness and partially reduce the beneficial effects of the amorphous W-Al layers.

Coatings incorporating a central W-N layer exhibited brittle fracture with extensive spallation along the scratch track, regardless of the microstructure of the nitride (see Fig. 3(d) and (e)). The presence of both conformal and buckling cracks along the tracks indicates relatively poor cohesive properties and limited toughness compared to the W-Al coatings, consistent with the high hardness and low plasticity of nitride materials.

Finally, the W-Cr-Ti coated sample showed a relatively smooth scratch track with limited edge cracking and no evidence of large-scale lateral spallation (see Fig. 3(f)). Although conformal and buckling cracks were still observed, the overall response suggests better accommodation of substrate plasticity and improved stress distribution compared to the W–N coatings.

Using the approach proposed by Benjamin and Weaver [44], the interfacial shear stresses were preliminarily estimated considering the Rockwell indenter geometry (200 μm tip radius), the critical loads associated with coating delamination (Lc2) and the corresponding penetration depths (see Table 1). For all samples, the calculated values are around 0.5 GPa, indicating robust resistance to tangential stresses, despite differences in composition, number of layers or microstructure. These results suggest that the substrate–interlayer interface, common to all coatings, primarily governs interfacial bonding, whereas variations in multilayer architecture mainly influence mechanical compliance, the ability to accommodate stresses and barrier performance. The deposition of a pure W interlayer under a synchronized pulsed substrate bias of

Table 1
Summary of scratch test results for W-based coatings.

Sample ID	Lc1 [N]	Lc2 [N]	Lc3 [N]	Penetration depth at Lc2 [μm]	Shear Stress [GPa]
pure W	1.4	3.4	5.3	10.88	0. 497
W-Al#3	4.9	9	15	29.1	0. 492
W-Al#7	3.6	3.9	13.1	12.46	0.498
W-N#C	3	4.6	7.8	9.25	0.499
W-N#A	1.3	3.1	11.4	9.9	0.498
W-Cr-Ti	1.4	2.9	6.5	14.8	0.495

800 V promotes energetic ion bombardment, increasing adatom mobility and creating near-atomically contact, which results in a high density of atomic bonds across the interface. This strategy effectively decouples shear resistance from barrier performance: the W interlayer ensures robust interfacial bonding, while multilayer composition and architecture can be optimized independently for corrosion resistance and mechanical robustness.

Fig. 4 compares the performance of W-Al#3 and W-Al#7 coatings after corrosion tests in liquid Sn at 400 °C. The W-Al#3 coating, with a smaller number of alternating layers, either provided complete protection or displayed only localized corrosion spots (see Fig. 4(a) and (b)), consistent with previous observations [27]. These corroded regions are limited in size, typically tens to a few hundred microns in radial extension. Despite the localized penetration of liquid Sn and the partial loss of the original substrate, the coating remained in its original position and kept its composition (see Fig. 4(c.1-c.5)), indicating low residual stress and chemical compatibility with the liquid metal. This, in addition to the formation of corrosion products, likely acted as a partial barrier, slowing down further dissolution. Differently, both W-Al#7 coated samples resulted intact under the same experimental conditions (see Fig. 4(d) and (e)). The higher number of alternating layers, at comparable total thickness, enhanced overall coating robustness, which was not affected by contact with liquid Sn (see Fig. 4(f.1-f.5)).

This architecture provides multiple and sequential barriers, offering a higher level of reliability in the event of partial layer failure. If the first layer is locally compromised, subsequent layers interrupt or retard corrosion propagation. Additionally, the alternation of amorphous and crystalline layers acts as a "shell-like" barrier, where the failure of one layer does not immediately compromise the integrity of the overall coating. This arrangement not only hinders liquid metal diffusion but may also improve mechanical properties by deflecting cracks and accommodating local stresses. Therefore, the comparison demonstrates that increasing the number of layers within a given total thickness can be a highly effective strategy to improve resistance to liquid metal corrosion. This approach combines chemical inertness, mechanical robustness and a multiple barrier effect, which together significantly enhance the protective performance of W-Al multilayer coatings. The results also suggest that careful design of multilayer architecture, considering both the number and type of individual layers, can be as important as the choice of materials themselves when developing coatings for high-temperature liquid metal environments.

The comparison between W-N#C and W-N#A coated samples

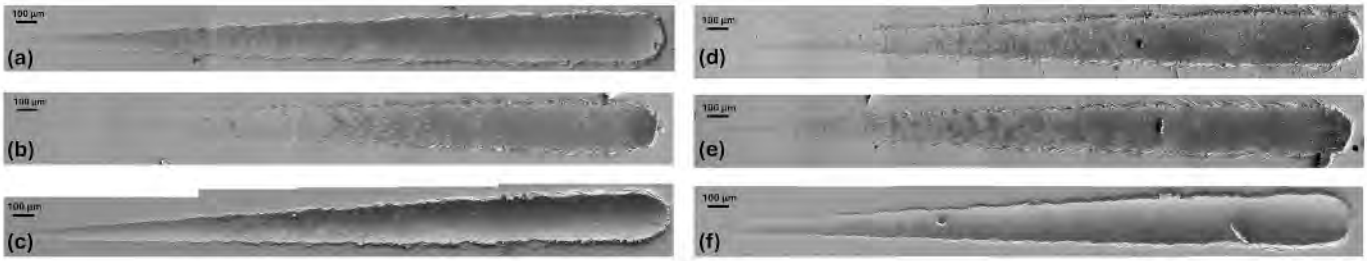

Fig. 3. SEM images of the scratch track of (a) W, (b) W-Al#3, (c) W-Al#7, (d) W-N#C, (e) W-N#A and (f) W-Cr-Ti coatings.

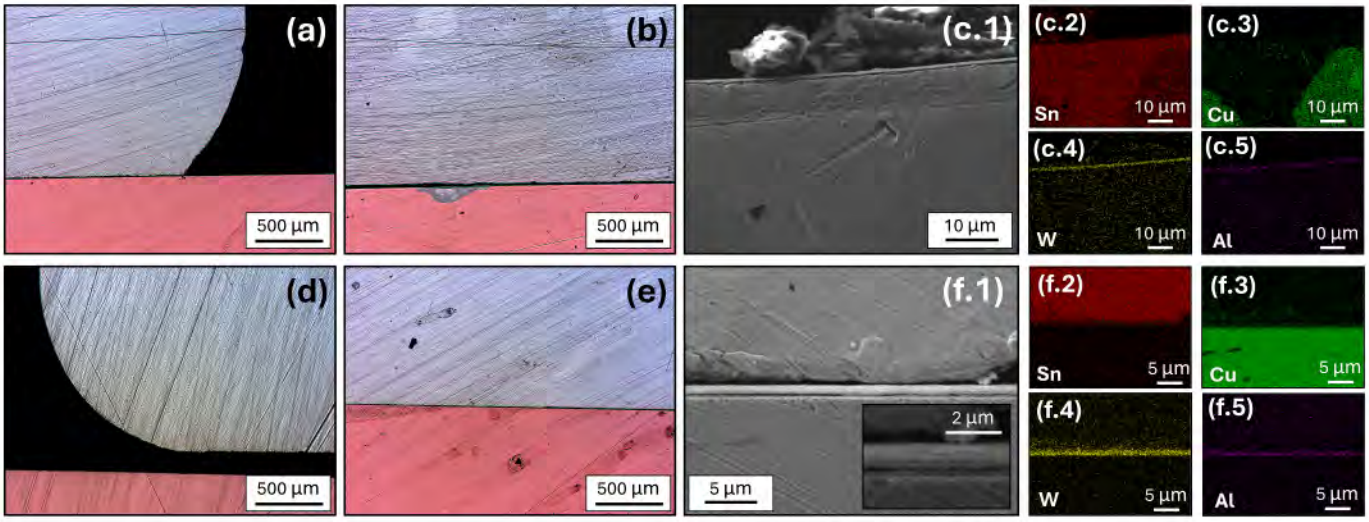

Fig. 4. Optical and SEM characterization of corrosion-tested W-Al coatings. W-Al#3 coated samples: the CuCrZr substrate was either **(a)** unaffected or **(b)** locally corroded by liquid Sn. In the latter case, **(c.1)** SEM cross-sectional images and **(c.2–c.5)** EDS elemental maps show that the coating largely maintained its original position despite partial substrate dissolution. W-Al#7 coated samples: the CuCrZr substrate remained **(d–e)** uncorroded by liquid Sn. **(f.1)** SEM cross-sectional images and **(f.2–f.5)** EDS maps confirm the absence of interaction between the substrate and liquid Sn. The inset of panel **(f.1)** highlights that the multilayer architecture of the coating remained essentially unchanged after corrosion test. The following colour code was adopted for the various elements: Sn (red), Cu (green), W (yellow), Al (magenta). (For interpretation of the references to colour in this figure legend, the reader is referred to the web version of this article.)

highlights the critical influence of the microstructure of the central layer on corrosion performance. As illustrated in Fig. 5(a) and (b), the W-N#C coating, containing a crystalline W-N central layer, failed in all experiments. As a result, extensive formation of Cu-Sn intermetallic compounds (IMCs) and widespread substrate dissolution took place (see Fig. 5(c.1-c.4)).

Once the CuCrZr substrate was locally removed, the brittle crystalline W-N layer collapsed in other regions due to thermal stress, lack of substrate support and the thermal expansion mismatch between the ceramic-like W-N and the metallic substrate. This brittle failure mode is markedly different with the behaviour of the full metallic W-Al system, whose mixed layer may possess a coefficient of thermal expansion (CTE) closer to that of CuCrZr, allowing it to better accommodate thermal strains and maintain adhesion even when the underlying substrate is locally corroded. In contrast, the W-N#A coating, featuring an amorphous central W-N layer, demonstrated superior performance, with either no attack or only localized corrosion spots similar to W-Al#3 coatings (see Fig. 5(d) and (f.1-f.4)). This clear difference between W-N#C and W-N#A coatings demonstrates that, despite containing the same constituent elements, the microstructure of the mixed layer plays a decisive role in determining the protective effectiveness. The absence of grain boundaries in the amorphous structure likely suppresses fast diffusion paths that would otherwise accelerate Sn penetration in the crystalline counterpart, thus improving the barrier properties and delaying liquid metal penetration. Furthermore, the amorphous layer may exhibit higher tolerance to localized stresses, reducing the likelihood of brittle cracking. However, the W-N#A coating frequently exhibited partial delamination from the substrate after corrosion test,

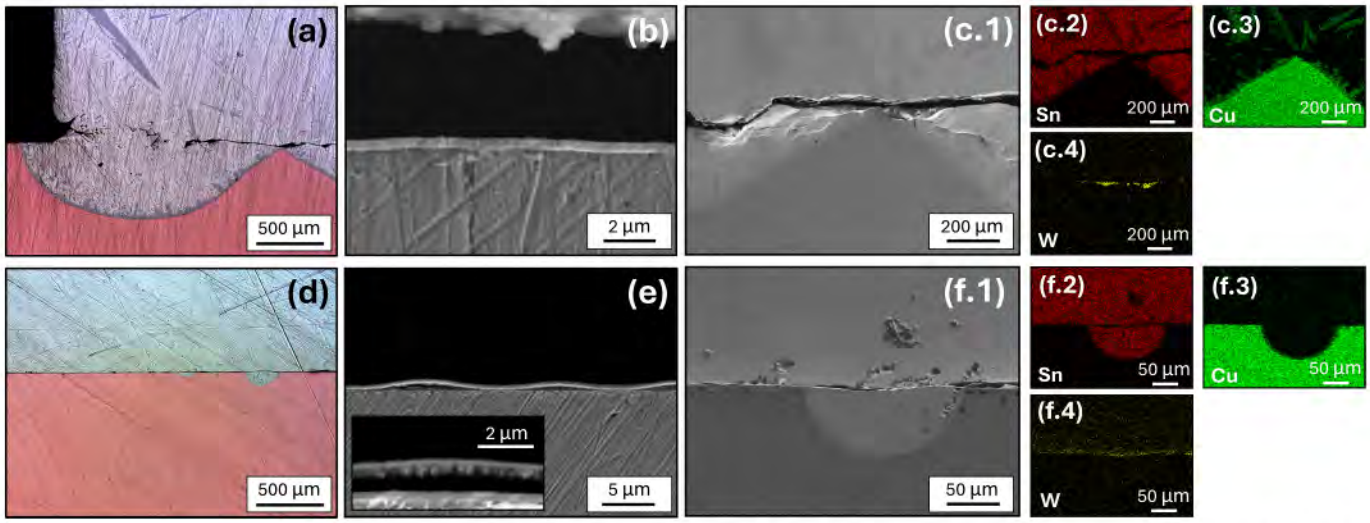

Fig. 5. Optical and SEM characterization of corrosion-tested W-N coatings. W-N#C coated samples: the CuCrZr substrate was **(a)** severely corroded by liquid Sn, although **(b-c.1)** the coating remained locally recognizable. **(c.2-c.5)** EDS maps reveal extensive IMC formation within the Sn droplet. W-N#A coated samples: the CuCrZr substrate was either unaffected or **(d)** locally corroded. **(e)** In both cases, partial coating detachment from the substrate was observed after testing, as highlighted by the inset. (f.1) SEM cross-sectional images and **(f.2–f.5)** EDS maps confirm the limited extent of substrate dissolution where Sn attack occurred. The following colour code was adopted for the various elements: Sn (red), Cu (green), W (yellow). (For interpretation of the references to colour in this figure legend, the reader is referred to the web version of this article.)

even when the substrate remained intact (see Fig. 5(e)). This phenomenon can likely be attributed to two concurrent processes: (i) atomic rearrangement or partial recrystallization in the amorphous layer induced by heating at 400 °C; (ii) the intrinsic mismatch in CTE between W-N and the CuCrZr substrate may have resulted in stresses upon cooling, ultimately driving detachment at the interface. Such behaviour raises concerns regarding the long-term reliability of this coating architecture, particularly under reactor-relevant conditions where repeated heating–cooling cycles and solid–liquid transitions of the liquid metal are expected in the CPS environment. These results underline the importance of complementing static corrosion tests with dedicated thermal cycling experiments and post-exposure mechanical adhesion measurements to fully assess the thermomechanical compatibility of candidate coatings under service-relevant conditions.

The behaviour of the W-Cr-Ti coating under liquid Sn exposure showed divergent outcomes. Among the two nominally identical samples, one experienced extensive corrosion, while the other remained intact (see Fig. 6(a) and (d), respectively). In the corroded sample, significant growth of Cu–Sn IMCs occurred (see Fig. 6(a) and (c.1-c.6)). Despite this, the multilayer structure of the coating remained distinguishable in SEM images (see Fig. 6(b)). The top and bottom pure W layers appear brighter, while the central multielement layer is darker, consistent with the presence of lighter elements such as Ti and Cr. Lower-magnification images confirm the presence of the detached coating, with observed curvature suggesting residual stresses from deposition (see Fig. 6(c.1–c.6)). Notably, the EDS analysis of the coating shows a weak or elusive signal for Ti and Cr, in contrast to the dominant W signal. This differs from the W-Al system, where Al is readily detectable. While partial dissolution of Ti and Cr into liquid Sn could be hypothesized, literature indicates that their solubility under the tested temperatures and exposure times is extremely limited [45,46]. A more plausible explanation involves mechanical effects. During cross-sectional preparation, local deformation may preferentially expose the top or bottom W layers, which partially shielded the X-ray emission from Ti and Cr. Additionally, the crystalline nature of the W-Cr-Ti layer likely amplified the deformation effect. Unlike the amorphous W-Al mixed layer, the crystalline structure may fracture differently under mechanical stress, influencing EDS signal detection. Conversely, the twin sample did not show corrosion, confirming that the constituent materials are chemically compatible with liquid Sn under the tested conditions (see Fig. 6(e) and (f.1-f.6)). Nevertheless, the fully crystalline central layer may result in less predictable performance when the coating does not achieve uniform or complete coverage. Local substrate surface irregularities can exacerbate this variability, explaining why one sample failed while the other survived. Residual stresses may further compromise the performance. Indeed, following localized attack, the coating may be unable to maintain mechanical integrity, leading to additional cracking and facilitating liquid Sn penetration. Compared to the W-N#C coating, the W-Cr-Ti system exhibits higher variability, likely because the central mixed layer possesses a CTE more compatible with the substrate, partially mitigating local delamination. When combined with other amorphous or compliant layers, such a multilayer architecture could offer a balanced compromise between mechanical robustness and chemical resistance.

Role of coating thickness and substrate roughness

Fig. 7(a–d) show cross-sectional SEM micrographs of W-Al#3 coatings with different central layer thicknesses. In all cases, the W-Al layer exhibits a featureless, compact and dense morphology, unaffected by thickness variations. Since the thickness of the bottom and top W films was kept constant for all samples, the results confirm that W-Al morphology remains stable and does not evolve toward columnar or crystalline structures with increasing thickness. Each W-Al#3 coating was deposited on CuCrZr substrates with different surface finishes. Representative surface morphologies of the adopted substrates at high and low magnification are shown in Fig. 7(e).

Fig. 8 illustrates the surface appearance of W-Al#3 coatings deposited on CuCrZr substrates. The analysis focuses on the two extreme cases, namely the thinnest (Fig. 8(a), (c), and (d)) and the thickest coatings (Fig. 8(b), (e), and (f)). For substrates with low roughness (R_a), the coatings exhibit optimal and uniform coverage. However, as the substrate roughness increases (R_a = 0.5 or 1 μm), both the uniformity and homogeneity of the deposited layer tend to decrease. The local morphology of the coating becomes increasingly influenced by the underlying substrate topography. For instance, near the edges of machining marks, the coating appears less compact and smooth. Indeed, the planar surface exhibits a ripple-like nanostructure, likely resulting from the directional growth following the irregularities of the substrate. These morphological features are already evident for the thinnest coating at R_a = 0.5 μm. In contrast, for the thickest coating, such inhomogeneities start to become noticeable at the same roughness, but

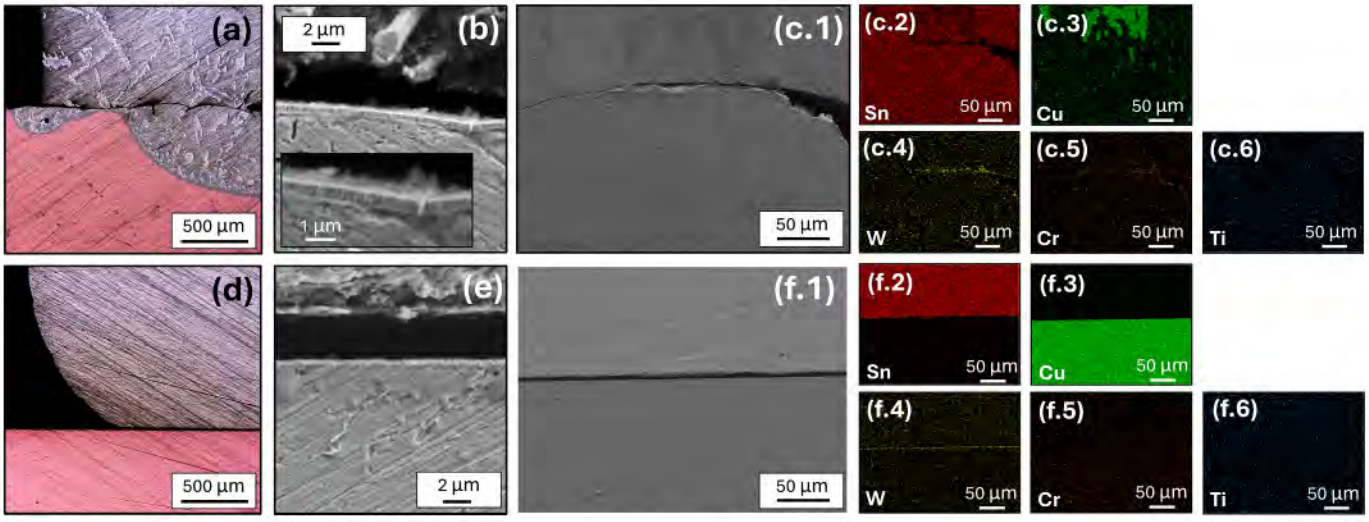

Fig. 6. Optical and SEM characterization of corrosion-tested W-Cr-Ti coatings. **(a)** The first sample was severely corroded by liquid Sn, although **(b–c.1)** the coating remained locally recognizable. The inset in panel **(b)** highlights the multilayer architecture through grayscale contrast. **(d–f.1)** The second sample showed no visible degradation after the test. EDS analyses confirm the markedly different behaviour of **(c.2–c.5)** corroded and **(f.2–f.5)** intact samples. In both cases, the W signal is clearly detectable, whereas Cr and Ti signals appear comparatively weaker. The following colour code was adopted for the various elements: Sn (red), Cu (green), W (yellow), Cr (orange), Ti (blue). (For interpretation of the references to colour in this figure legend, the reader is referred to the web version of this article.)

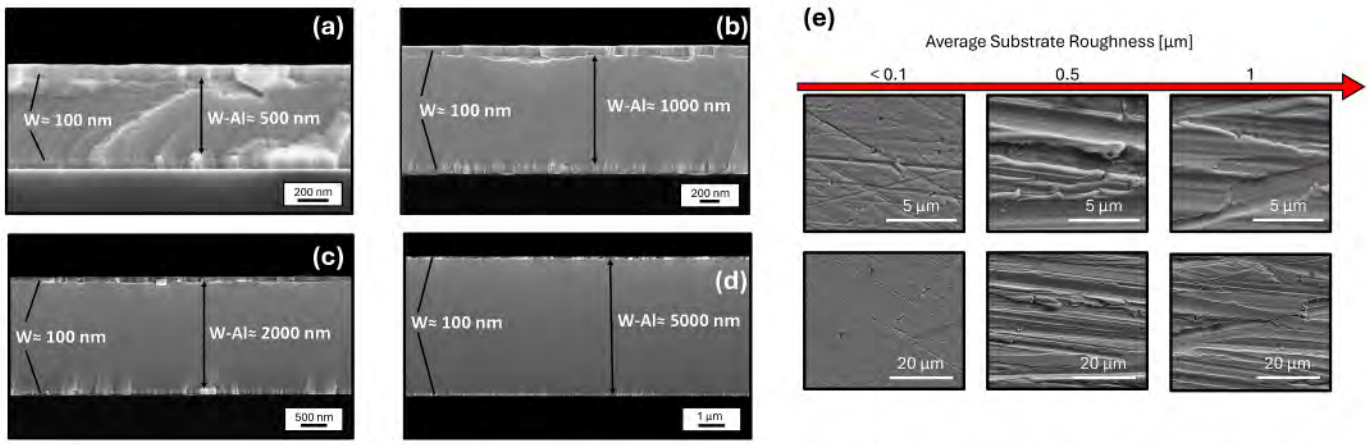

Fig. 7. SEM cross-sectional morphology of W-Al#3 coatings with a thickness of the central layer of (a) 0.5, (b) 1, (c) 2 and (d) 5 µm, respectively. (e) High and low magnification SEM images of CuCrZr substrates illustrating the planar surface morphology corresponding to different finishing treatments.

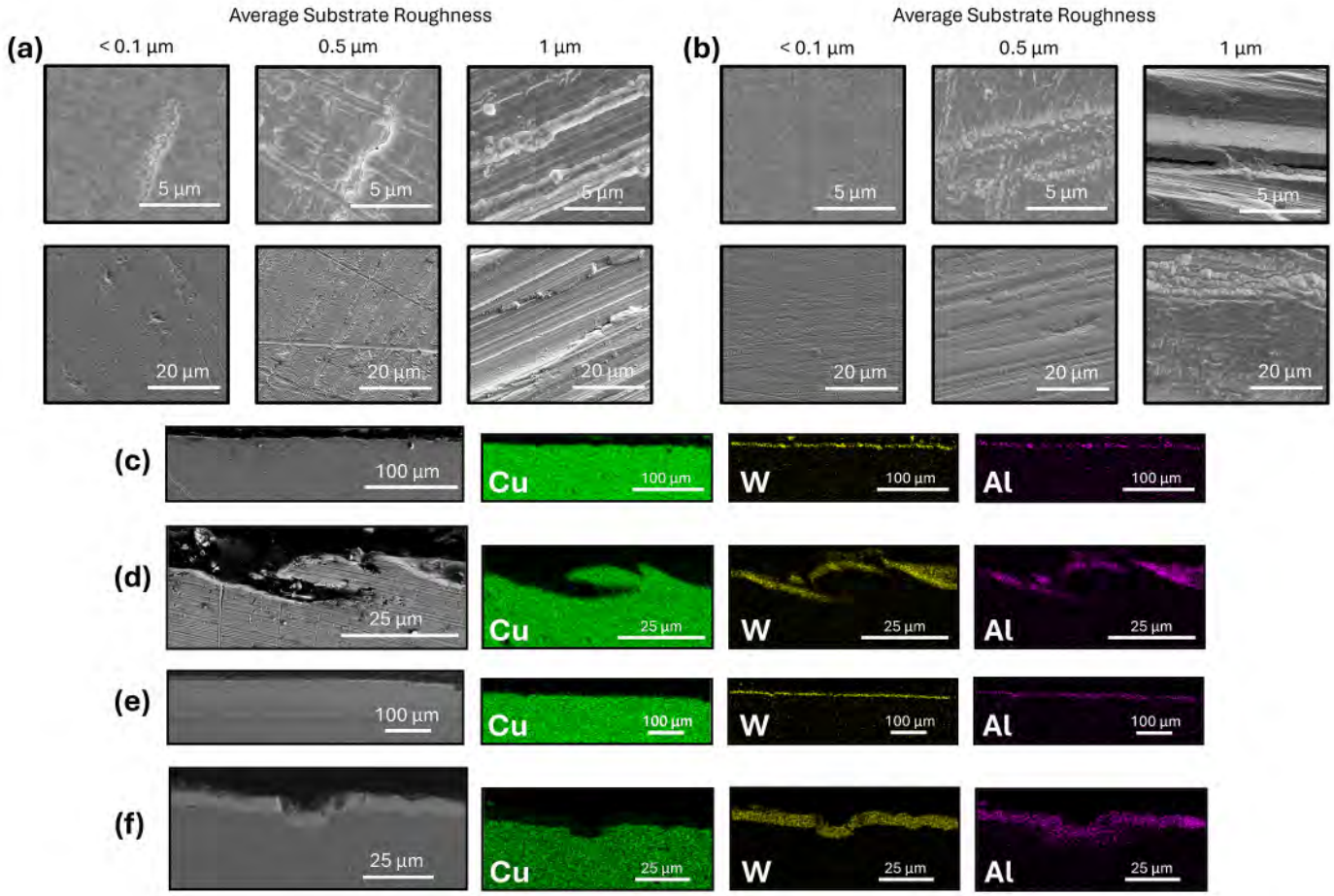

Fig. 8. High and low magnification SEM planar views of CuCrZr substrates with different roughness coated with (a) a 0.5 µm-thick and (b) a 5 µm-thick W-Al#3 coating. Cross-sectional SEM images of the $R_a = 1$ µm substrate coated with (c,d) the 0.5 µm-thick and (e,f) the 5 µm-thick W-Al#3 coating. The following colour code was adopted for each element: Cu (green), W (yellow), Al (magenta). The following colour code was adopted for the various elements: Cu (green), W (yellow), Al (magenta). (For interpretation of the references to colour in this figure legend, the reader is referred to the web version of this article.)

they are more clearly defined when the substrate roughness reaches $R_a = 1$ µm. Thus, increasing the coating thickness is necessary to achieve conformal coverage of substrates with significant surface irregularities, particularly when the latter approaches the scale of typical industrial finishes. This is especially relevant for PVD technologies, where process optimization is required to avoid excessively long deposition times. However, it is important to note that increasing thickness alone cannot guarantee optimal coverage in the presence of pronounced substrate topography. In regions where the substrate geometry creates shadowed areas, conformal deposition becomes challenging. This is particularly critical for relatively ductile materials like CuCrZr, which can undergo local plastic deformation during surface machining. The high-magnification image of the $R_a = 1$ µm substrate coated with the thickest layer exemplifies this, showing a substrate gap only partially

covered. Despite the advantages of HiPIMS deposition, such as the generation of highly ionized metallic species that follow electric field lines (in both grounded and biased configurations) toward the substrate and promote superior step coverage, physical obstacles induced by substrate topography cannot be fully compensated. This observation is corroborated by the cross-sectional inspection of the roughest substrates. Low-magnification images for both the thinnest and thickest coatings (see Fig. 8(c) and (e), respectively) reveal apparently uniform coverage. However, higher magnification clearly shows that local substrate features may hinder the formation of a continuous coating layer (see Fig. 8(d)). This discontinuity can compromise the protective performance under liquid–metal exposure, where even small uncoated regions may act as initiation sites for corrosion. As mentioned above, increasing coating thickness can mitigate this effect by improving coverage of non-planar areas (see Fig. 8(f)). Nevertheless, when surface asperities become very large, as evident in Fig. 8(d), the required coating thickness increases significantly, raising concerns about compatibility with typical PVD deposition rates and process times.

Coating deposited on lowest roughness substrates ($R_a < 0.1$ μm) were considered for scratch test experiments. The progressive evolution of the scratch tracks reported in Fig. 9 and the critical loads summarized in Table 2 highlight a strong dependence of the failure mechanisms on the thickness of the central W–Al layer within the multilayer architecture. Additional EDS images of the scratch tracks are provided in the Supplementary Material. At the lowest W–Al thickness (see Fig. 9(a)), the coating exhibited extensive delamination and spallation along the scratch path, with large exposed regions of the CuCrZr substrate. Failure proceeded mainly through buckling-driven cracking, where residual stress exceeded the interfacial adhesion strength, leading to localized debonding. The coating fractured into relatively large fragments, indicating good internal cohesion but, at the same time, limited strain accommodation and a brittle response typical of rigid refractory coatings on ductile substrates. This behaviour can be ascribed to the non-negligible contribution of the top and bottom pure W layers to the total thickness of the multilayer.

When the W–Al layer thickness was increased to 1 μm (see Fig. 9(b)), the coating showed improved mechanical integrity, although buckling and localized spallation remained visible near the edges of the scratch. Cracks became finer and more regularly spaced, suggesting partial stress relaxation and more homogeneous energy dissipation during sliding. The delamination fronts appeared less extended, reflecting a moderate improvement in adhesion. A similar trend was observed for the coating containing the 2 μm-thick W–Al layer (see Fig. 9(c)), where a further reduction in the exposed CuCrZr substrate area indicates a better balance among mechanical properties, residual stress, and interfacial strength.

For the thickest W–Al layer (see Fig. 9(d)), the coating preserved its structural coherence over almost the entire tested region. Most of the track length showed no cracks or tensile arc cracks, while conformal or buckling cracks appeared only near the end of the scratch where substrate exposure occurred. Globally, the coating followed the deformation imposed by the indenter without significant delamination, demonstrating a transition from brittle interfacial failure to a more ductile and energy-absorbing response. This behaviour suggests that increasing the W–Al layer thickness enhances the compliance of the multilayer, mitigating stress localization and promoting crack deflection and arrest within the coating rather than at the interface. Notably, at the beginning of the track, partial detachment of the top W layer was observed, whereas the underlying mixed layer remained adherent to the substrate (see Section A.2 in Supplementary Material). This further supports the interpretation that the rigidity and brittleness of the pure W layers are counterbalanced by the ductile-like behaviour of the amorphous W–Al layer, whose beneficial effect becomes increasingly evident as it represents a larger fraction of the multilayer thickness.

Table 2
Summary of scratch test results for W–Al#3 coatings with different central layer thicknesses.

W-Al layer thickness [μm]	Lc1 [N]	Lc2 [N]	Lc3 [N]	Penetration depth at Lc2 [μm]	Shear Stress [GPa]
0.5	3.5	3.6	7.8	11.5	0. 498
1	4.9	9	15	29.1	0. 492
2	5.9	11.9	17.2	38.35	0.494
5	6.5	23	23.9	74.47	0.492

The measured critical loads (Lc2) were used to estimate interfacial shear stresses according to the Benjamin–Weaver equation. As in paragraph 3.1, values around 0.5 GPa were obtained for all samples (see Table 2). This indicates that shear resistance is consistently governed by the common pure W interlayer, prepared with a pulsed 800 V substrate bias. Thus, while the variation in amorphous layer thickness strongly affects the ability to accommodate stresses, the interfacial bonding remains robust, effectively decoupling adhesion from barrier performance.

The produced samples were subjected to corrosion tests in contact with liquid Sn at 500 °C, following the experimental setup described in Section 2.2. Fig. 10(a.1-a.3) shows the macroscopic appearance of CuCrZr substrates with varying surface roughness coated with W-Al#3 films approximately 2 μm thick, representative of the cases observed across all corrosion tests. The complete set of post-test sample images is provided in Section A.3 of Supplementary Material.

Regardless of the W-Al#3 coating thickness, all samples with high surface roughness ($R_a \approx 1$ μm) exhibited severe corrosion, as exemplified in Fig. 10(a.1). The Sn droplet remained firmly adhered to the substrate surface and displayed a jagged morphology, indicative IMCs formation due to the interaction between Cu and liquid Sn. This observation is corroborated by SEM-EDS analyses shown in Fig. 10(b.1-b.3). In particular, both at the droplet/substrate interface and within the droplet, Cu-enriched regions corresponding to distinct Cu-Sn intermetallic phases can be identified [47]. Compositional measurements indicate that the ϵ phase (Cu_3Sn, ≈ 25–30 at.% Sn / ≈ 70–75 at.% Cu) forms at the droplet/substrate interface, whereas the η phase (Cu_6Sn_5, ≈ 45.5 at.% Sn / ≈ 54.5 at.% Cu) appears as elongated structures within the droplet. The more pronounced growth of Cu-Sn intermetallics at 500 °C compared to 400 °C [27] highlights the strong temperature dependence of interdiffusion between liquid Sn and the Cu-based substrate. While the thermodynamic driving force for IMCs formation remains largely unchanged across this temperature range, the enhanced atomic mobility at 500 °C significantly accelerates IMCs layer growth. From a materials compatibility perspective, this accelerated formation of IMCs implies an increased corrosive potential of liquid Sn, as it promotes faster substrate consumption and earlier compromise of structural integrity.

Consequently, even minor defects or locally uncovered regions of the substrate become far more critical at 500 °C than at 400 °C. This explains

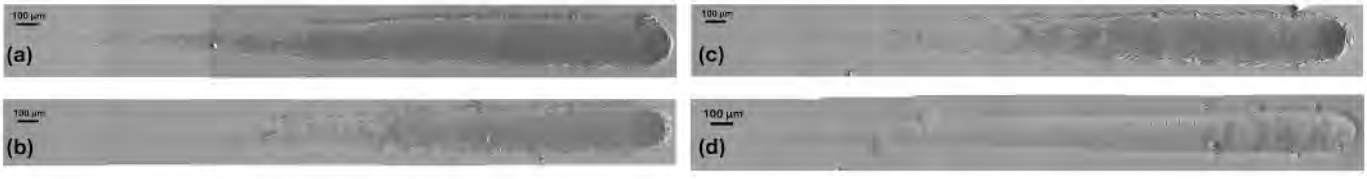

Fig. 9. SEM images of the scratch track of W-Al#3 coatings with a thickness of the central layer of (a) 0.5, (b) 1, (c) 2 and (d) 5 μm, respectively.

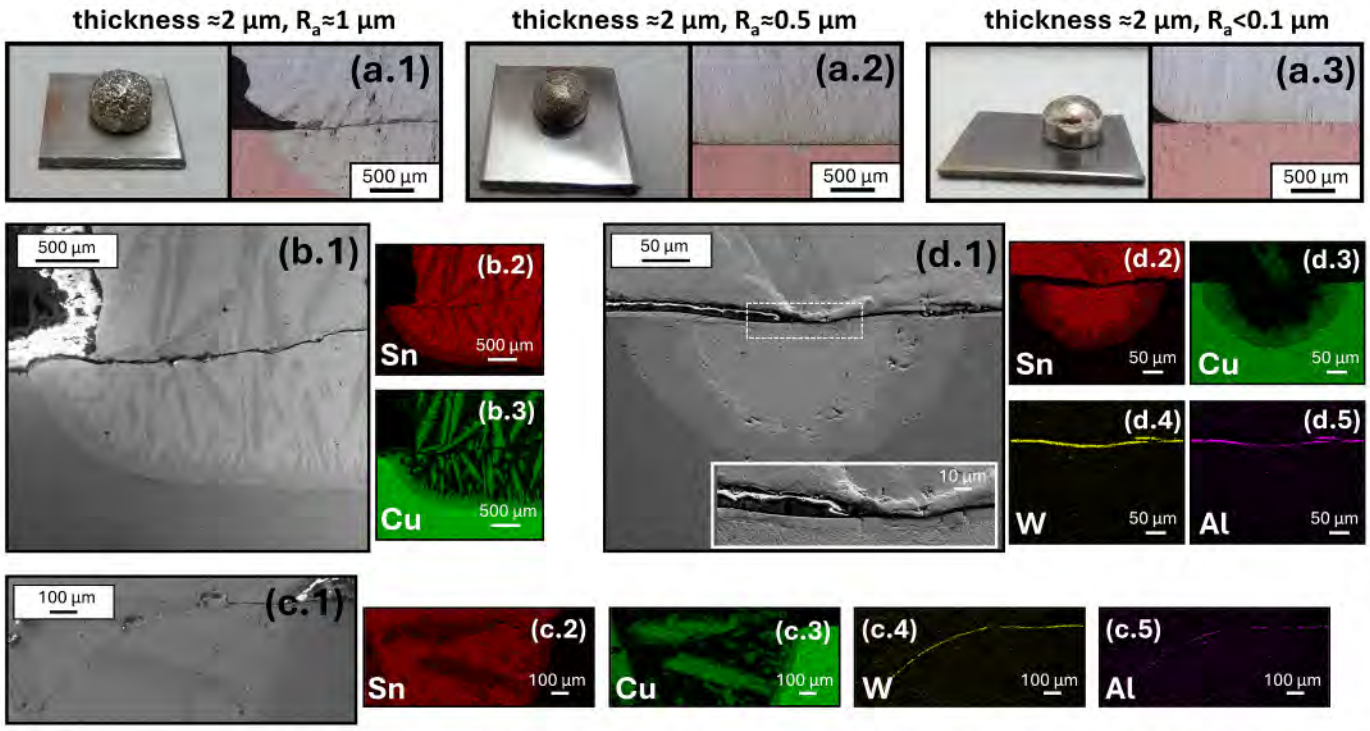

Fig. 10. Macroscopic appearance of CuCrZr substrates with different surface roughness coated with a W-Al#3 coating of approximately 2 μm: **(a.1)** fully corroded sample, **(a.2)** partially corroded sample and **(a.3)** non-corroded sample after exposure to liquid Sn at 500 °C for 600 min. **(b.1-b.3)** SEM cross-sectional images and EDS elemental maps of a fully corroded sample, highlighting the extensive formation of Cu–Sn IMCs both at the substrate/droplet interface and within the solidified Sn droplet. **(c.1-c.5)** Higher-magnification cross-sections of the corroded region, showing that the W-Al#3 coating remains recognizable and partially adherent despite substrate dissolution. **(d.1-d.5)** SEM cross-sections and EDS maps of a sample exhibiting localized corrosion, with damage confined to a limited area and the coating maintaining its structural integrity over the void left by the dissolved substrate. The following colour code was adopted for the various elements: Sn (red), Cu (green), W (yellow), Al (magenta). (For interpretation of the references to colour in this figure legend, the reader is referred to the web version of this article.)

why all samples coated with W-Al#3 films approximately 0.5 μm thick suffered severe corrosion, despite promising results on substrates with surface finishes below 0.1 μm were obtained [27]. At the higher temperature, defects that previously caused only localized corrosion now result in extensive substrate dissolution. Interestingly, despite the penetration of liquid Sn, the W-Al#3 coating remains identifiable and, where possible, adherent to the original substrate surface (see Fig. 10 (c.1-c.5)). This observation confirms that the coating material itself is chemically inert to liquid Sn, even at elevated temperatures.

Considering other W-Al#3 coating thicknesses and substrates with intermediate or low roughness ($R_a \approx 0.5$ μm or < 0.1 μm), specimens exhibited also partial or localized corrosion appearing as in Fig. 10(a.2) after the tests. Fig. 10(d.1-d.5) illustrates such cases, where corrosion spots are spatially confined within regions ranging from tens to a few hundred microns in radius. In these areas, the coating largely maintained its original position despite partial dissolution of the underlying substrate. Notably, the structural integrity of the coating, remaining unbroken and largely planar after substrate removal, helped to slow liquid Sn penetration and prolong confinement of the corrosive process, thereby providing a secondary protective effect. It is worth noting that nominally identical samples exhibited markedly different behaviours, ranging from complete to partial corrosion, and in some cases even no corrosion at all. The latter case can already be recognized at the macroscopic level, as the Sn droplet, once solidified, retained a smooth and shiny appearance (see Fig. 10(a.3)). This observation further confirms that the onset of corrosion is not primarily dictated by the coating composition itself, but rather by its local quality and conformity, which strongly depends on the underlying substrate surface. Even when the nominal roughness is identical, small-scale irregularities or machining defects can significantly hinder conformal coverage by the coating, creating localized sites that are particularly vulnerable to liquid Sn attack. The only set of samples that displayed no visible signs of corrosion consisted of substrates with $R_a < 0.1$ μm coated with the thickest W-Al#3 layer (≈ 5 μm). Fig. 11 summarizes results concerning this set of samples. As shown in Fig. 11(a), the Sn droplet easily detached from the substrate after solidification, indicating the absence of significant interaction with the CuCrZr surface. This is consistent with the lack of detectable Cu-Sn IMCs within the droplet, confirming that no appreciable diffusion or chemical reaction occurred during exposure. The W-Al#3 coating appears continuous, well adherent and distinguishable from the underlying substrate, which remained unaffected by the corrosion test (Fig. 11(b.1-b.5)). A higher-magnification cross-sectional view (Fig. 11(c)) provides further insight into the coating microstructure after exposure. The three individual layers of the multilayer architecture (i.e, the bottom W layer, the central W-Al layer and the top W layer) are clearly recognizable, particularly in the upper region of the image where the coating fractured during mechanical cross-sectioning. This unintentional fracture highlights the internal morphology of the coating and allows a more precise observation of layer interfaces. Notably, the interface between the top W layer and the W-Al layer remains sharp and well-defined, with no evidence of interdiffusion or interfacial reactions even after 600 min at 500 °C. Despite the prolonged high-temperature exposure, the layer retained its featureless, compact and dense morphology, with no visible segregation, recrystallization or grain coarsening that could compromise its barrier properties. This observation suggests that the mixed W-Al layer possesses excellent structural and chemical stability under thermal conditions relevant to liquid metal applications, a crucial requirement for ensuring long-term protection of Cu-based heat sink materials in high-heat-flux environments.

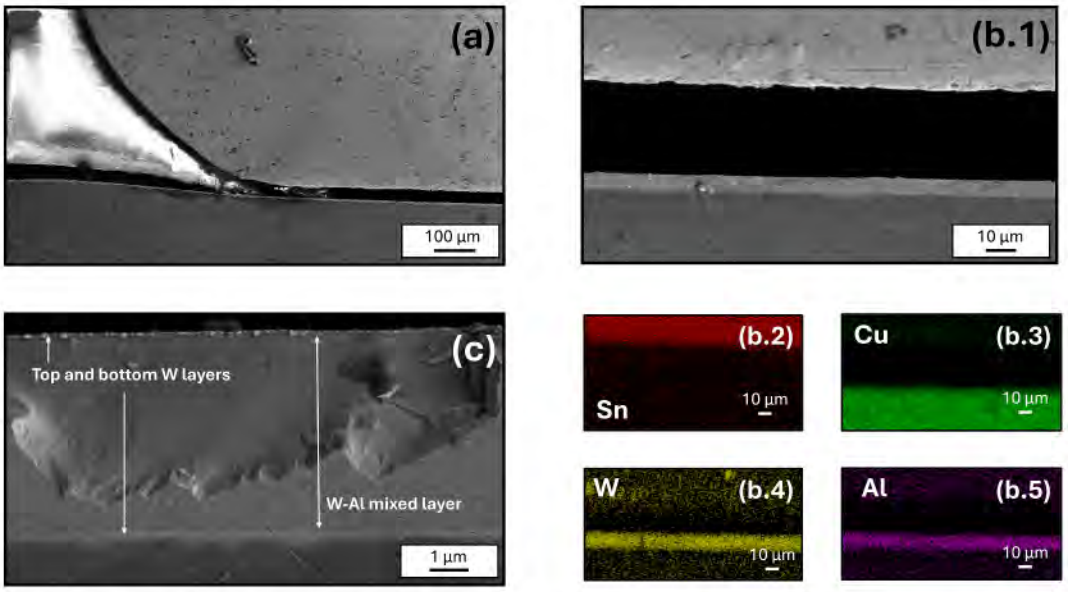

Fig. 11. (a) SEM cross-sectional image of a CuCrZr substrate with $R_a < 0.1$ µm coated with a 5 µm-thick W-Al#3 layer after exposure to liquid Sn for 600 min at 500 °C. The Sn droplet is completely detached from the surface, confirming the absence of Cu-Sn interaction. (b.1-b.5) Higher-magnification cross-sectional view and corresponding EDS maps, evidencing the lack of intermetallic formation and substrate dissolution. (c) Detailed view of the coating morphology after exposure, showing the three-layer architecture (bottom W layer, central W-Al layer, and top W layer) with sharp interfaces. The following colour code was adopted for the various elements: Sn (red), Cu (green), W (yellow), Al (magenta). (For interpretation of the references to colour in this figure legend, the reader is referred to the web version of this article.)

General discussion and implications for liquid metal divertor

The results of this work provide an integrated view of key parameters governing the performance of W-based coatings developed for liquid metal divertor applications. Indeed, the corrosion performance emerges from a coupled effect of coating chemical composition, microstructure, architecture, thickness and the surface state of the substrate. Additionally, controlling adhesion and resistance to tangential stresses through tailored deposition and interface engineering is crucial, especially when substantial mechanical mismatches exist between the coating and the substrate [35–38]. This highlights the need for a comprehensive approach that simultaneously addresses materials science and engineering challenges when designing protective barriers for fusion-relevant components.

Firstly, the excellent intrinsic chemical compatibility of W-based coatings with liquid Sn was confirmed, in agreement with previous results regarding both bulk [48–50] and surface deposited materials [5,27]. Across all tested conditions, W-based layers remained inert, with no evidence of interdiffusion or dissolution. Therefore, coating failure was consistently associated with morphological or mechanical factors (e.g., insufficient coverage, local discontinuities or stress relaxation) rather than with chemical degradation of the coating material itself. This result validates the choice of W-based systems as suitable candidates for long-term operation in a liquid Sn-based divertor. In this respect, these materials may also be of interest in the case of liquid Li, another candidate for liquid metal divertor applications where, similarly to the Sn case, compatibility issues affect Cu-based substrates and refractory materials show promising chemical stability [5,24,25,51]. Within this framework, the use of refractory-based coatings appears particularly relevant, especially considering that the stability of standard oxide-based coatings such as alumina has been reported to be affected by liquid Li [52].

Moreover, a central outcome of this study is the superior behaviour of coatings that incorporate amorphous mixed layers (W-Al#1, W-Al#3, W-N#A), which consistently exhibited either no attack or only highly localized penetration of liquid Sn at 400 °C. The absence of grain boundaries in these layers likely suppresses preferential diffusion paths for the liquid metal, delaying corrosion onset. The enhanced toughness of the amorphous layers, inferred from the progressive failure patterns observed in the scratch tests, provides an explanation for these observations. Specifically, the W-Al#3 and W-Al#7 coatings displayed block-like cracking and relatively high critical loads, demonstrating their ability to dissipate stresses and accommodate substrate plasticity. This mechanical compliance supports the corrosion results, as it allows the coating to remain adherent and intact even when localized substrate dissolution occurs. Multilayer architectures with alternating amorphous and crystalline layers further enhanced robustness by creating sequential diffusion barriers and improving mechanical compliance [53–55], effectively preventing complete coating failure even in the presence of local damage. These findings are consistent with prior observations in liquid metal-based fission-relevant systems [56–58], underscoring amorphization as a powerful strategy to mitigate high-temperature corrosion and delay catastrophic failure.

Corrosion experiments also revealed the importance of balancing microstructural stability and residual stress, even in chemically resistant coatings. W–N#C or W-Cr-T coated samples showed lower Lc values and more extensive spallation, confirming that brittleness amplify vulnerability under combined mechanical and chemical loading. As a consequence, coatings featuring a fully crystalline central layer showed either systematic failure or inconsistent behaviour, with one of two nominally identical W-Cr-Ti samples undergoing complete corrosion. These divergent results suggest that crystalline mixed layers are more sensitive to local substrate finishing, coating continuity and residual stress state. Once local penetration occurs, the brittle nature of these layers and the plausible mismatch in CTE with CuCrZr promote crack propagation and accelerate coating failure [59–61]. The scratch tests corroborate this, as W–N#C and W-Cr-Ti coatings exhibited conformal and buckling cracks along the track, indicating limited cohesive strength and reduced strain accommodation. These observations underline the need for improved process control during deposition to ensure conformal coverage, as well as the potential benefit of integrating more compliant or amorphous interlayers to relieve stress and accommodate strain during operation.

From an engineering perspective, the presented results shed light on the practical considerations that must guide the transition from proof-of-

concept studies to divertor-relevant components. Coating systems that can maintain adhesion and structural integrity after localized attack are highly desirable, as they prevent uncontrolled exposure of the substrate and slow down corrosion kinetics. However, the partial delamination observed for W–N#A coating even in the absence of substrate dissolution raises concerns about thermomechanical compatibility under the cyclic conditions expected in a liquid metal divertor, where repeated heating, cooling and solidification events will impose additional stresses at the coating-substrate interface. Systematic thermal cycling and post-exposure mechanical adhesion tests emerge as essential next steps in the qualification of candidate coatings.

The complementary study on coating thickness and substrate roughness provides additional and crucial information.

While the W-Al layer retained a dense and featureless morphology independent of thickness, corrosion experiments clearly showed that insufficient thickness or poor substrate preparation can critically affect protective performance. Scratch tests confirmed this trend: thinner W-Al layers exhibited extensive buckling, spallation and substrate exposure, whereas thicker layers transitioned toward energy-absorbing and ductile-like responses, with higher critical loads and fewer catastrophic failures. This behaviour is not always observed in protective coatings for harsh environments, where increasing thickness can sometimes lead to a deterioration of either protective performance or mechanical response [62,63]. On rougher substrates ($R_a \approx 1$ µm), severe corrosion occurred regardless of coating thickness, confirming that local topographic irregularities create shadowed regions where coverage is incomplete. These sites act as preferential initiation points for liquid metal attack, particularly as the kinetic of Cu-Sn IMC formation is accelerated at 500 °C. This is consistent with the variability observed even among nominally identical samples, where microscopic differences in surface features dictated whether a given specimen failed, partially degraded or remained intact. Increasing coating thickness improves conformal coverage and delays failure, but cannot fully compensate for extreme roughness or deep machining marks. Therefore, controlling substrate finish emerges as a key technological requirement for achieving reproducible corrosion protection. In particular, a compromise on substrate roughness becomes essential even when using advanced PVD techniques such as HiPIMS, which can ensure good step coverage. The main limitation in this case is not uniformity [64,65], but the need for increasingly thick coatings to cover pronounced surface asperities, which significantly extends deposition times and may become impractical for large-scale components [66,67].

Importantly, the results also highlight a secondary protective function of the W-Al coating. Even after localized substrate dissolution, the coating frequently preserved its integrity and remained in place, further slowing penetration of liquid Sn. This effect suggests that, beyond acting as a chemical barrier, the coating can mechanically confine the corrosive process, providing additional time before structural integrity is compromised. From a design perspective, this is a valuable property, as it implies a mode of progressive failure, allowing the coating to maintain partial protective capability rather than undergoing a sudden loss of performance.

Conclusions

This work provides a comprehensive framework for the design and qualification of protective coatings for liquid metal divertor applications. Specifically, the reported results highlight scientific and technological parameters that critically affect coating performance in ensuring chemical compatibility between liquid Sn and Cu-based structural materials.

Firstly, W-based coatings systems, and particularly W-Al ones, demonstrated to combine chemical inertness with microstructural stability, even after prolonged exposure at 500 °C. In this respect, the presence of amorphous morphologies represents a promising strategy for suppressing fast diffusion paths of the liquid metal and delaying the onset of IMCs growth.

Secondly, the study highlighted the value of multilayer architectures. Indeed, alternating crystalline and amorphous layers not only act as sequential diffusion barriers, but also improve the mechanical response and partially preserve the integrity of the barrier even after local substrate dissolution. This behaviour, while not preventing eventual failure, allows a degree of controlled degradation that slows substrate consumption and prolongs protection.

Lastly, substrate preparation and coating thickness were identified as relevant engineering parameters. While moderate roughness may contribute to mechanical interlocking at the interface, excessive substrate roughness leads to coating discontinuities and defect formation, which become preferential sites for liquid metal attack. Therefore, adequate surface finishing is mandatory to minimize local defects that act as preferential attack sites, whereas sufficient coating thickness ensures conformal coverage even on moderately rough industrial surfaces. However, process feasibility requires practical limits on achievable thicknesses, especially for PVD techniques such as HiPIMS. This suggests that future optimization must balance coating performance with deposition rate and scalability.

Future work should focus on thermal cycling and transient loading experiments, as well as adhesion improvement, to bridge the gap between laboratory experiments and reactor-relevant conditions, ultimately enabling reliable development of liquid metal divertor in fusion reactors. In this respect, the study of coating response to irradiation under external ion fields, combined with corrosion testing, represents a crucial step for future investigations.

CRediT authorship contribution statement

D. Vavassori: Writing – review & editing, Writing – original draft, Visualization, Methodology, Investigation, Formal analysis, Data curation, Conceptualization. **L. Bana:** Writing – review & editing, Writing – original draft, Methodology, Investigation, Formal analysis, Data curation, Conceptualization. **M. Bugatti:** Writing – review & editing, Writing – original draft, Methodology, Investigation, Formal analysis, Data curation, Conceptualization. **F. Zarotti:** Writing – review & editing, Investigation. **N. Lecis:** Writing – review & editing, Investigation. **M. Iafrati:** Writing – review & editing, Supervision, Project administration, Conceptualization. **M. Passoni:** Writing – review & editing, Supervision, Resources, Project administration. **L. Ferrante:** Writing – review & editing, Supervision, Project administration, Investigation, Conceptualization. **D. Dellasega:** Writing – review & editing, Supervision, Project administration, Methodology, Investigation.

Declaration of competing interest

The authors declare that they have no known competing financial interests or personal relationships that could have appeared to influence the work reported in this paper.

Acknowledgements

This work has been carried out within the framework of the EUROfusion Consortium, funded by the European Union via the Euratom Research and Training Programme (Grant Agreement No 101052200 — EUROfusion). Views and opinions expressed are however those of the author(s) only and do not necessarily reflect those of the European Union or the European Commission. Neither the European Union nor the European Commission can be held responsible for them.

Appendix A. Supplementary data

Supplementary data to this article can be found online at https://doi.org/10.1016/j.nme.2026.102116.

Data availability

Data will be made available on request.

References

[1] Liquid Metal Cooled Reactors: Experience in Design and Operation (TECDOC Series (CD-ROM) 1569). Vienna: INTERNATIONAL ATOMIC ENERGY AGENCY, 2008, isbn: 978-92-0-152208-5.

[2] D. Gorse-Pomonti, V. Russier, Liquid metals for nuclear applications, J. Non Cryst. Solids 353 (32–40) (2007) 3600–3614, https://doi.org/10.1016/j.jnoncrysol.2007.05.175.

[3] L. Zhang, C. Deng, X. Ji, X. Liu, Liquid metals power advanced nuclear energy systems, The Innovation (2025).

[4] T.W. Morgan, P. Rindt, G.G. van Eden, V. Kvon, M.A. Jaworksi, N.J.L. Cardozo, Liquid metals as a divertor plasma-facing material explored using the Pilot-PSI and Magnum-PSI linear devices, Plasma Phys. Controlled Fusion 60 (1) (2017) 014025, https://doi.org/10.1088/1361-6587/aa86cd.

[5] J. Hu, et al., Recent progress in the development of liquid metal plasma facing components for magnetic fusion devices, Nucl. Mater. Energy 41 (2024) 101776, https://doi.org/10.1016/j.nme.2024.101776 issn: 2352-1791.

[6] G. Maddaluno, D. Marzullo, G. Mazzitelli, S. Roccella, G. Di Gironimo, R. Zanino, The DTT device: Divertor solutions for alternative configurations including liquid metals, Fusion Eng. Des. 122 (2017) 341–348, https://doi.org/10.1016/j.fusengdes.2017.03.172, issn: 0920-3796.

[7] V. Pericoli Ridolfini, R. Ambrosino, P. Chmielewski, F. Crisanti, M. Poradziński, R. Zagórski, Perspectives for the liquid lithium and tin targets in the Italian Divertor Test Tokamak (I-DTT) divertor, Nucl. Fusion 59 (12) (2019) 126008, https://doi.org/10.1088/1741-4326/ab3969.

[8] R. Ambrosino, "DTT - Divertor Tokamak Test facility: A testbed for DEMO," Fusion Engineering and Design, vol. 167, p. 112 330, 2021, issn: 0920-3796. doi: 10.1016/j.fusengdes.2021.112330.

[9] J. W. Coenen et al., "Materials for DEMO and reactor applications-boundary conditions and new concepts," Physica Scripta, vol. 2016, no. T167, p. 014 002, 2015. doi: 10.1088/0031-8949/2016/T167/014002.

[10] S. Roccella, G. Dose, R. de Luca, M. Iafrati, A. Mancini, G. Mazzitelli, CPS based liquid metal Divertor Target for EU-DEMO, J. Fusion Energ. 39 (6) (2020) 462–468, https://doi.org/10.1007/s10894-020-00263-4.

[11] P. Rindt, J. van den Eijnden, T. Morgan, N. Lopes Cardozo, Conceptual design of a liquid-metal divertor for the European DEMO, Fusion Eng. Des. 173 (2021) 112812, https://doi.org/10.1016/j.fusengdes.2021.112812 issn: 0920-3796.

[12] G. Nallo, G. Mazzitelli, M. Moscheni, F. Subba, R. Zanino, SOLPS-ITER simulations of a CPS-based liquid metal divertor for the EU DEMO: Li vs Sn, Nucl. Fusion 62 (3) (2022) 036008, https://doi.org/10.1088/1741-4326/ac4867.

[13] R. Nygren, F. Tabarés, Liquid surfaces for fusion plasma facing components-a critical review. Part I: Physics and PSI, Nucl. Mater. Energy 9 (2016) 6–21, https://doi.org/10.1016/j.nme.2016.08.008, issn: 2352-1791.

[14] F. Tabarés, E. Oyarzabal, A. Martin-Rojo, D. Tafalla, A. de Castro, A. Soleto, Reactor plasma facing component designs based on liquid metal concepts supported in porous systems, Nucl. Fusion 57 (1) (2016) 016029, https://doi.org/10.1088/0029-5515/57/1/016029.

[15] E. Oyarzabal, et al., Comparative study of different Sn wetted W CPSs exposed to NBI fluxes in the OLMAT facility, Fusion Eng. Des. 190 (2023) 113711, https://doi.org/10.1016/j.fusengdes.2023.113711 issn: 0920-3796.

[16] M. Baldwin, R. Doerner, S. Luckhardt, R. Conn, Deuterium retention in liquid lithium, Nucl. Fusion 42 (11) (2002) 1318, https://doi.org/10.1088/0029-5515/42/11/305.

[17] P. Fernandez-Mayo, E. Oyarzabal, I. Fernandez-Berceruelo, Parametric study of the thermal response of liquid tin-tungsten capillary porous systems exposed to high thermal loads, Fusion Eng. Des. 220 (2025) 115372, https://doi.org/10.1016/j.fusengdes.2025.115372 issn: 0920-3796.

[18] J.G.A. Scholte, et al., Liquid metal droplet ejection through bubble formation under hydrogen plasma and radical exposure, J. Fusion Energ. 44 (1) (2025) 1–27.

[19] M. Kondo, M. Yukihiro, Y. Kitamura, M. O, and T. Tanaka, "Corrosion mechanism of reduced activation ferritic martensitic steel JLF-1 in liquid metal Sn," Corrosion Science, vol. 209, p. 110 748, 2022. doi: 10.1016/j.corsci.2022.110748.

[20] A. Heinzel, A. Weisenburger, G. Müller, Corrosion behavior of austenitic steel AISI 316L in liquid tin in the temperature range between 280 and 700 °C, Mater. Corros. 68 (8) (2017) 831–837, https://doi.org/10.1002/maco.201609211.

[21] Y. Miyakawa, M. Kondo, Corrosion behaviors of various steels and nickel-based alloys in liquid Sn media, Nucl. Mater. Energy 30 (2022) 101154, https://doi.org/10.1016/j.nme.2022.101154 issn: 2352-1791.

[22] L. Snugovsky, M.A. Ruggiero, D.D. Perovic, J.W. Rutter, Experiments on interaction of liquid tin with solid copper, Mater. Sci. Technol. 19 (7) (2003) 866–874, https://doi.org/10.1179/026708303225002794.

[23] D. Zhang, et al., Study of the corrosion characteristics of 304 and 316L stainless steel in the static liquid lithium, J. Nucl. Mater. 553 (2021) 153032, https://doi.org/10.1016/j.jnucmat.2021.153032 issn: 0022-3115.

[24] C. D. Moynihan, S. Stemmley, B. Moore, R. Trendler, M. A. Hossain, and D. N. Ruzic, "Characterization of liquid lithium corrosion for fusion reactor materials," Fusion Engineering and Design, vol. 199, p. 114 102, 2024, issn: 0920-3796. doi: 10.1016/j.fusengdes.2023. 114102. [Online]. Available: https:// www.sciencedirect. com/ science/ article/ pii/ S0920379623006816.

[25] X. Meng, et al., Corrosion characteristics of copper in static liquid lithium under high vacuum, J. Nucl. Mater. 513 (2019) 282–292, https://doi.org/10.1016/j.jnucmat.2018.10.037, issn: 0022-3115.

[26] J.S. Hu, et al., A review of lithium application for the plasma-facing material in EAST Tokamak, Rev. Mod. Plasma Phys. 7 (1) (2023) 9.

[27] D. Vavassori, et al., Corrosion resistance of HiPIMS tungsten and tungsten-aluminium coatings in contact with liquid Sn, Surf. Coat. Technol. 494 (2024) 131449, https://doi.org/10.1016/j.surfcoat.2024.131449 issn: 0257-8972.

[28] M. Bugatti, L. Bana, D. Vavassori, M. Iafrati, D. Dellasega, M. Passoni, Progress in the development of a W-based Corrosion Barrier for ENEA liquid Sn-based divertor design, J. Fusion Energ. 44 (2025), https://doi.org/10.1007/s10894-025-00503-5.

[29] S. Stemmley, B. Moore, C. Moynihan, O. Yang, K. Skrecky, D.N. Ruzic, Contact angle measurements of liquid lithium on surface-modified stainless steel, insulating materials, and other metals and coatings, Fusion Eng. Des. 208 (2024) 114649, https://doi.org/10.1016/j.fusengdes.2024.114649 issn: 0920-3796.

[30] W. Zhang et al., "Research progress on LBE corrosion-resistant coatings: A review," Progress in Nuclear Energy, vol. 176, p. 105 358, 2024, issn: 0149-1970. doi: 10 .1016 /j.pnucene.2024.105358.

[31] J. Ni, et al., Study of CrAl coatings fabricated by HiPIMS with enhanced resistance to LBE corrosion, Surf. Coat. Technol. 513 (2025) 132476, https://doi.org/10.1016/j.surfcoat.2025.132476 issn: 0257-8972.

[32] M. Ammendola, et al., Evaluation of chromium coatings deposited by standard and bipolar high-power impulse magnetron sputtering (HiPIMS & B-HiPIMS) for nuclear power applications, Surf. Coat. Technol. 485 (2024) 130835, https://doi.org/10.1016/j.surfcoat.2024.130835 issn: 0257-8972.

[33] M.S. Galli De Magistris, et al., Corrosion behaviour in liquid lead of pristine and irradiated FeCrAlNi coatings deposited by HiPIMS, Materials & Desing 260 (2025) 114923, https://doi.org/10.1016/j.matdes.2025.11492.

[34] J. Yang et al., "Influence of coating thickness on microstructure, mechanical and LBE corrosion performance of amorphous AlCrFeTiNb high-entropy alloy coatings," Surface and Coatings Technology, vol. 441, p. 128 502, 2022, issn: 0257-8972. doi: 10 .1016 / j.surfcoat.2022.128502.

[35] B. Navinšek, P. Panjan, J. Krušic, Hard coatings on soft metallic substrates, Surf. Coat. Technol. 98 (1998) 809–815, https://doi.org/10.1016/S0257-8972(97)00316-2.

[36] Y. D. Zhu et al., "Surface Modification of C17200 Copper-Beryllium Alloy by Plasma Nitriding of Cu-Ti Gradient Film," Journal of Materials Engineering and Performance, vol. 27, pp. 961-969, 201, doi: 10.1007/s11665-018-3190-4.

[37] Y. Zhu, et al., Effects of the prefabricated Cu-Ti film on the microstructure and mechanical properties of the multiphase coating by thermo plasma nitriding on C17200 Cu alloy, Coatings 9 (2019) 694, https://doi.org/10.3390/coatings9110694.

[38] A.V. Kolubaev, et al., Structure and properties of CrN/TiN multilayer coatings produced by cathodic Arc plasma deposition on copper and beryllium-copper alloy, Phys. Mesomech. 25 (2022) 306–317, https://doi.org/10.1134/S102995992204004X.

[39] D. Lundin, J. T. Gudmundsson, and T. Minea, High Power Impulse Magnetron Sputtering: Fundamentals, Technologies, Challenges and Applications. Elsevier, 2020, isbn: 9780128124543. doi: 10.1016/C2016-0-02463-4.

[40] D. Vavassori, F. Mirani, F. Gatti, D. Dellasega, M. Passoni, Role of magnetic field and bias configuration on HiPIMS deposition of W films, Surf. Coat. Technol. 458 (2023) 129343, https://doi.org/10.1016/j.surfcoat.2023.129343 issn: 0257-8972.

[41] L. Bana, D. Vavassori, G. Marra, D. Dellasega, and M. Passoni, "Energetic ions for the growth of amorphous and crystalline tungsten-nitrogen layers by HiPIMS," Surface and Coatings Technology, vol. 514, p. 132 544, 2025, issn: 0257-8972. doi: 10 .1016 / j.surfcoat.2025.132544.

[42] L. Bana, T. Moroni, G. Marra, D. Dellasega, M. Passoni, Microstructure control in WCrTi medium-entropy alloy coatings by HiPIMS-induced ionization, MRS Adv. (2025) 1–7, https://doi.org/10.1557/s43580-025-01277-w.

[43] D. Dellasega, F. Mirani, D. Vavassori, C. Conti, M. Passoni, Role of energetic ions in the growth of fcc and ω crystalline phases in Ti films deposited by HiPIMS, Appl. Surf. Sci. 556 (2021) 149678, https://doi.org/10.1016/j.apsusc.2021.149678 issn: 0169-4332.

[44] P. Benjamin, C. Weaver, Measurement of adhesion of thin films, Proc A (1960) 163–176, https://doi.org/10.1098/rspa.1960.0012.

[45] A. Bouhajib, A. Nadiri, A. Yacoubi, R. Castanet, Partial enthalpies of titanium, hafnium, tantalum, tungsten and iridium in liquid tin at high dilution, Journal of Alloys and Com-pounds 287 (1) (1999) 170–173, https://doi.org/10.1016/S0925-8388(99)00048-1, issn: 0925-8388.

[46] A. Yassin, R. Castanet, Enthalpies of dissolution of elements in liquid tin: II. Transition, alkali and alkaline-earth metals, J. Alloy. Compd. 314 (1) (2001) 160–166, https://doi.org/10.1016/S0925-8388(00)01228-7, issn: 0925-8388.

[47] A. Leineweber, The Cu–Sn system: a comprehensive review of the crystal structures of its stable and metastable phases, J. Phase Equilib. Diffus. 44 (3) (2023) 343–393, https://doi.org/10.1007/s11669-023-01041-3.

[48] N. Kawano, Y. Tamai, M. Kondo, Excellent Corrosion Resistance of Tungsten Materials in liquid Tin, Plasma and Fusion Research 15 (2020) 1205068, https://doi.org/10.1585/pfr.15.1205068.

[49] A. Vertkov, I. Lyublinski, M. Zharkov, G. Mazzitelli, M. Apicella, M. Iafrati, Liquid tin limiter for FTU tokamak, Fusion Eng. Des. 117 (2017) 130–134, https://doi.org/10.1016/j.fusengdes.2017.01.041.

[50] M. Kondo, et al., "Conceptual design of HFIR irradiation experiment for material compatibility study on liquid Sn divertor," Plasma and Fusion Research, vol. 16, p. 2405040, doi: 10.1585/pfr.16.2405040.

[51] D.H. Zhang, et al., Study on corrosion behavior of 3D-printing W and WZrC in static liquid Li, J. Fusion Energ. 44 (2025) 17, https://doi.org/10.1007/s10894-025-00488-1.
[52] W. Lu, et al., Corrosion resistance of ceramic candidates for tritium permeation barriers exposed to molten lithium, Corros. Sci. 160 (2019) 108172, https://doi.org/10.1016/j.corsci.2019.108172.
[53] C.L. Chang, C.H. Huang, C.Y. Lin, F.C. Yang, J.F. Tang, Mechanical properties of amorphous and crystalline CrN/CrAlSiN multilayer coating fabricated using HPPMS, Surf. Interfaces 31 (2022) 102064, https://doi.org/10.1016/j.surfin.2022.102064 issn: 2468-0230.
[54] K. Yang, et al., Revealing microstructure and the associated corrosion mechanism of Al/amorphous Al2O3/Al tri-layer coating deposited on depleted uranium by magnetron sputtering, Appl. Surf. Sci. 659 (2024) 159911, https://doi.org/10.1016/j.apsusc.2024.159911 issn: 0169-4332.
[55] L. Zhao, et al., Construction and protection mechanism of CoCrFeNiTi/Ti amorphous–nanocrystalline multilayer coatings fabricated by magnetron sputtering, J. Alloy. Compd. 1039 (2025) 183135, https://doi.org/10.1016/j.jallcom.2025.183135 issn: 0925-8388.
[56] F. García Ferré, et al., The mechanical properties of a nanocrystalline Al2O3/a-Al2O3 composite coating measured by nanoindentation and Brillouin spectroscopy, Acta Mater. 61 (7) (2013) 2662–2670, https://doi.org/10.1016/j.actamat.2013.01.050, issn: 1359-6454.
[57] F. García Ferré, M. Ormellese, F. Di Fonzo, M. Beghi, Advanced Al2O3 coatings for high temperature operation of steels in heavy liquid metals: a preliminary study, Corros. Sci. 77 (2013) 375–378, https://doi.org/10.1016/j.corsci.2013.07.039, issn: 0010-938X.
[58] F. García Ferré, et al., Corrosion and radiation resistant nanoceramic coatings for lead fast reactors, Corros. Sci. 124 (2017) 80–92, https://doi.org/10.1016/j.corsci.2017.05.011.
[59] Y. Niu, et al., Preparation and thermal shock performance of thick α-Ta coatings by direct current magnetron sputtering (DCMS), Surf. Coat. Technol. 321 (2017) 19–25, https://doi.org/10.1016/j.surfcoat.2017.04.045, issn: 0257-8972.
[60] E. Besozzi, D. Dellasega, A. Pezzoli, A. Mantegazza, M. Passoni, M. Beghi, Coefficient of thermal expansion of nanostructured tungsten based coatings assessed by substrate curvature method, Mater. Des. 137 (2018) 192–203, https://doi.org/10.1016/j. matdes.2017.10.001, issn: 0264-1275.
[61] S. Xiao, et al., Evaluation of environmental barrier coatings: a review, Int. J. Appl. Ceram. Technol. 20 (4) (2023) 2055–2076, https://doi.org/10.1111/ijac.14370.
[62] J. Yang, et al., Influence of coating thickness on microstructure, mechanical and LBE corrosion performance of amorphous AlCrFeTiNb high-entropy alloy coatings, Surf. Coat. Technol. 441 (2022) 128502, https://doi.org/10.1016/j.surfcoat.2022.128502.
[63] F. Cao, et al., Influence of thickness and Ti interlayer on scratch and wear resistance of CoCrNi medium entropy alloy coatings, J. Mater. Eng. Perform. 34 (2025) 7386–7395, https://doi.org/10.1007/s11665-024-09723-w.
[64] F. Jiang, et al., Structure, mechanical and corrosion properties of TiN films deposited on stainless steel substrates with different inclination angles by DCMS and HPPMS, Surf. Coat. Technol. 292 (2016) 54–62, https://doi.org/10.1016/j.surfcoat.2016.03.007, issn: 0257-8972.
[65] D. Xie et al., "Deposition of titanium films on complex bowl-shaped workpieces using DCMS and HiPIMS," Surface and Coatings Technology, vol. 442, p. 128 192, 2022, Special Issue of Surface and Coatings Technology celebrating the pioneering research career of Professor Allan Matthews in the field of "Plasma-based Surface Engineering", issn: 0257-8972. doi: 10.1016/ j.surfcoat.2022.128192.
[66] J. Vetter, et al., Industrial application potential of high power impulse magnetron sputtering for wear and corrosion protection coatings, J. Appl. Phys. 134 (16) (Oct. 2023), https://doi.org/10.1063/5.0159292 issn: 0021-8979.
[67] J. Hnilica, P. Klein, M. Učík, S. Debnárová, J. Kluso, P. Vašina, On direct-current magnetron sputtering at industrial conditions with high ionization fraction of sputtered species, Surf. Coat. Technol. 487 (2024) 131028, https://doi.org/10.1016/j.surfcoat.2024.131028 issn: 0257-8972.